Available online at www.sciencedirect.com
SCIENCE DIRECT®
ELSEVIER
Nuclear Instruments and Methods in Physics Research A 524 (2004) 236–244
NUCLEAR INSTRUMENTS & METHODS IN PHYSICS RESEARCH Section A
www.elsevier.com/locate/nima

The spatial and energy response of a 3d architecture silicon detector measured with a synchrotron X-ray microbeam

John Morse[a,*], Christopher J. Kenney[a], Edwin M. Westbrook[a], Istvan Naday[b], Sherwood I. Parker[c]

[a] *Molecular Biology Consortium, Chicago, IL, USA*
[b] *Argonne National Laboratory, Argonne, IL, USA*
[c] *University of Hawaii, Honolulu, HI, USA*

Received 30 October 2003; accepted 7 January 2004

Abstract

3D processed silicon detectors offer several advantages over conventional, planar processed devices. The electric fields between the electrodes of a 3D detector are parallel to its surface, and for a given applied bias, stronger than those found in a planar device of equivalent dimensions. We have investigated the spatial response of a first generation 3D detector using a synchrotron X-ray microbeam as a probe. The microbeam was of cross-section $\sim 10\,\mu m$, commensurate with the dimensions of the electrode structures. The detector showed excellent charge collection, as verified by the energy spectra acquired at various probe positions. Variations in the energy spectra provided a sensitive indicator of the charge splitting that inevitably occurs at the boundaries between adjacent pixel cells, and for measuring the expected loss of sensitivity at the 3D electrodes themselves.

PACS: 29.40.Wk; 29.40.Gx; 87.66.Pm

Keywords: Detector; 3D; Silicon; X-ray

1. Introduction

'3D' architecture radiation detectors have been fabricated with electrodes perpendicular to the silicon wafer's surface, and penetrating entirely through the bulk of the silicon wafer. Fig. 1 shows a schematic representation of these detectors, which have a simple geometry comprising alternate arrays of n- and p-type column electrodes. This geometry should be contrasted with that of conventional planar detectors, in which the electrode structures are parallel to the surface of the detector material and limited by processing technology to depths within a few microns of the wafer surface(s). We plan to build a large pixel array detector for macromolecular crystallography

*Corresponding author. Current address: European Synchrotron Radiation Facility, 6, Jules Horowitz, BP 220, Grenoble Cedex, F-38043, France. Tel.: 746-88-21-26; fax: 746-88-20-34.
E-mail address: morse@esrf.fr (J. Morse).

0168-9002/$ - see front matter
doi:10.1016/j.nima.2004.01.058

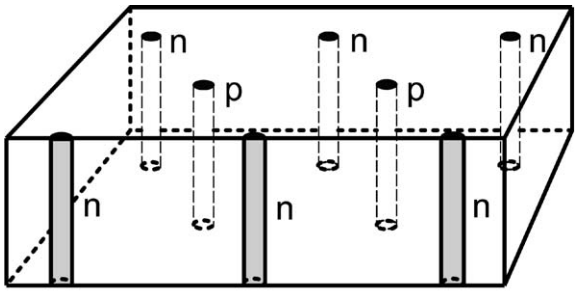

Fig. 1. Schematic of the 3D detector architecture, in which p and n electrodes traverse the entire bulk of a semiconductor material.

that will consist of several hundred, shingled 3D detectors, covering an area of at least $200 \times 200\,\mathrm{mm}^2$ [1]. The 3D architecture offers the following advantages in this application:

1. The spatial resolution of the detector is determined by the spacing between charge collecting column electrode centres, and the response at the boundaries of the individual charge collecting cells (pixels) themselves. At the energies $<15\,\mathrm{keV}$ corresponding to our intended application, X-ray absorption in silicon is dominated by the photoelectric effect. When an X-ray photon is absorbed, the ejected photoelectron thermalizes rapidly to create a charge cloud that drifts according to the local electric field, at the same time diffusing in three dimensions. If the X-ray is absorbed near the mid-point between adjacent like-sign electrodes, the charge generated splits and is collected by both neighbouring column electrodes. A similar situation arises in a planar processed detector, where the individual pixels are defined by (typically rectangular) electrodes fabricated at one surface of the detector. The extent of the spatial region between pixels over which significant charge sharing occurs depends upon several factors, in particular, the local electric field. Charge sharing in detectors that use a simple threshold scheme to detect individual X-ray photons may result in the false double counting of a single photon, or the recording of no count at all. For planar pixel detectors, this problem has been the subject of computational analysis [2] and several experimental studies [3–5]. As the electric fields between electrodes are parallel to the detector surface in 3D architecture detectors, charges are pulled away from rather than along pixel boundaries, and this reduces the spatial extent over which charge sharing is significant.
2. To produce large active area detectors, individual silicon detectors must be shingled or butt-jointed to create arrays. Planar detectors need a multiple guard ring structure at the cut edge of the silicon to control local electric field strength and thus avoid large surface leakage currents. For a tiled detector, the active area lost to adjacent peripheral guard rings creates an $X-Y$ grid of dead bands of width $\sim 500\,\mu\mathrm{m}$, typically wasting 5 to 10% of the total detector surface [6,7]. At the undulator X-ray sources of third generation synchrotrons, X-ray diffraction patterns from protein samples present many thousands of spots on the detector, of dimension $\sim 100\,\mu\mathrm{m}$ FWHM. Many of these spots will fall partly or wholly within the dead bands of a tiled detector, and these must be rejected from further analysis, reducing the completeness and overall quality of the data. In contrast, the 3D architecture detector has no vertical electric field component at its cut edges, and it is possible to process these detectors with edges that are themselves conductive, boundary electrodes. No guard rings are required for such 'active edges,' and the physical dicing of individual detectors from a parent silicon wafer using vertical plasma etching permits a dead margin of $<10\,\mu\mathrm{m}$ width around the periphery of the 3D detector. This makes feasible the assembly of large mosaic detector arrays with near zero dead area.

The initial concept, simulation [8], and fabrication [9] of silicon 3D detectors, and the particular architecture of the devices investigated here have already been reported [10]. By comparing the spectral energy response of the detectors to results of previous measurements made with ^{55}Fe and ^{241}Am flood sources, we confirmed that the detectors had not degraded significantly during

this period. It should be noted that the detectors used in the present study had been stored in air for two years with no particular precautions. The new measurements presented here were carried out using a synchrotron X-ray beam of cross-section $<10\,\mu m$ FWHM, which for the first time enabled us to study in detail the spatial response of the detectors. 3D detectors processed with active edges were not available for these tests, but measurements have been reported using an infrared probe beam on linear trench electrodes that were made to simulate such active edges [11].

2. The 3D detectors

The 3D detectors, with a matrix of 12×17 pixels covering an area $1.2 \times 3.2\,mm^2$, were fabricated from 121 μm thick silicon that had been fusion bonded to a 525 μm thick support wafer to facilitate processing. We have already shown that processed detectors can be removed from their support wafer, which is necessary to permit the rear side bump bonding of a CMOS readout circuits in a final, tiled array detector. Twelve sets of p-type column electrodes were electrically connected by an aluminium contact layer deposited on the detector surface to form parallel line segments. Electrical signals were measured at the end of these p electrode connection strips. Each column electrode extends completely through the silicon wafer and consists of a doped, polycrystalline silicon core from which dopant atoms have been diffused into the surrounding single-crystal silicon. The physical diameter of the polycrystalline silicon cores, as measured by optical microscopy, was 23 μm. Fig. 2 is a schematic representation of a fragment of the detector. The vertical separation between electrodes within a strip is 100 μm, and that between neighbouring strips of opposite electrode type is also 100 μm. As a result, for this detector the pixel charge collection area defined by the electric field is $100 \times 200\,\mu m^2$, centred on a p electrode, as depicted by the dotted rectangle in Fig. 2. The outermost, peripheral column electrodes of the detector (not shown in Fig. 2) were used to create three, parallel guard 'fences'. The middle of these

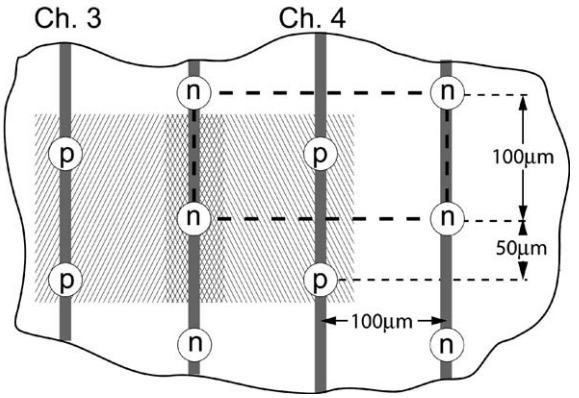

Fig. 2. Schematic of the 3DX detector tested. The grey vertical stripes represent the aluminium surface traces that connect the column electrodes. The overlapping, hatched rectangles correspond to the areas of the detector scanned while taking data from channel 3 and then channel 4.

three fences used n-type column electrodes, which were biased with all other n electrodes to the positive bias potential, while the outer and inner guard fences used p-type electrodes and were connected to ground. These guard fences were included as a precaution to collect leakage currents injected at the surface edges of the detector, as this was not processed with active edges, but simply diced from its parent silicon wafer by conventional saw cutting.

The 3D detector was mounted on a printed circuit board (PCB) support, and each of the p-type electrodes strips directly wire bonded to a charge-sensitive preamplifier channel of an adjacent silicon ASIC chip. Each of the ASIC preamplifier channels included a CR-RC shaping filter, with rise/fall times that were approximately 0.6/2 μs. As shown in Fig. 3, this detector-preamplifier assembly was itself piggyback mounted onto a second PCB that provided multiplexer circuitry to access any one of the 16 instrumented channels. This permitted successive measurement of the output of each channel under remote computer control using a single multichannel analyser (MCA) system. A NIM spectroscopy amplifier with a Gaussian shaping time of 2 μs was used to provided extra signal gain and restore large dc offsets of the ASIC. As pole zero compensation was not possible with this

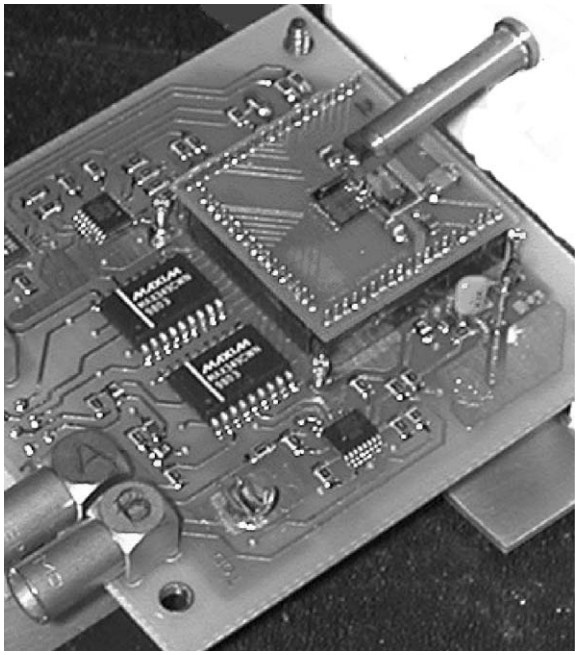

Fig. 3. The 3DX detector mounted on the readout board with 8-channel preamplifier-shaper ASIC and channel select signal multiplexer. The cylinder in the top right corner is a 0.4 MBq ^{55}Fe source which was used to make a flood X-ray illumination test of the detector before the beamline scans.

arrangement the signal amplification was non-optimal, resulting in large signal pulse undershoot. However, all data was acquired at low count rates (<7 kcps), which ensured little degradation from pulse pile-up artefacts.

As a preliminary to the beamline measurements, two detectors were laboratory tested using a flood field of X-rays from a ^{55}Fe radioactive source. The X-ray spectra obtained were qualitatively identical to those obtained from the same detectors two years earlier [10], with an energy resolution $\sim$0.9 keV FWHM, dominated by the preamplifier electronic noise. The best of these detectors depleted at 5 V bias, as evidenced by the plateau in its $I-V$ curve, and its total leakage current was 7 μA at an ambient temperature of 23°C and operating bias of 20 V. This large bias current was attributed to surface currents collected by the guard fence, as good X-ray spectra would have been impossible to measure if significant currents ($>$ nanoampere) had been flowing to the sensing column electrodes themselves. Previous current probe measurements made on three, 3D detectors taken from the same production batch had shown leakage currents of 0.6 to 1.3 nA mm^{-3}.

3. Beamline tests

Beamline tests were carried out at the GSE-CARS bending magnet beamline at the Advanced Photon Source, Argonne National Laboratory. The energy chosen for the X-ray beam used to characterize the 3D detector was 12.65 keV. This corresponds to the K-shell binding energy of selenium, which is of particular importance in the Multiple-wavelength Anomalous Dispersion technique now widely used in protein diffraction experiments. The BM13D beamline has a two crystal, silicon [1,1,1] monochromator. The second crystal was detuned, both to adjust the beam intensity and to suppress transmission of the third-order harmonic though the monochromator. As the 3D detector absorption efficiency was only $\sim$2% at the third harmonic energy 38 keV, the effect of residual beam harmonic pollution was negligible.

The spatial profile of the X-ray beam after its passage through a set of Fischer precision slits [12] was first measured. The Fischer horizontal (X) and vertical (Y) slits consisted of close spaced pairs of polished, tungsten carbide cylinders of 2 mm radius. The fixed spacing of each cylinder pair was tapered, so that by displacement of the X and Y pair using micrometer drives, the resultant crossed slit aperture could be adjusted in size from near zero to 100 μm square. X and Y scans of the X-ray beam profile were made by microstepping a 10 mm thick, honed-surface tungsten carbide block through the beam at the precise distance downstream from the slits where the 3D detector was later mounted. The block was tilted by $\sim5°$ to present a knife edge to the beam axis, thus avoiding glancing reflections from its surface. Fixed behind this moving knife edge, a YAP:Ce scintillation counter monitored the transmitted beam intensity. The slits were adjusted to give, at the position of the 3D detector, X and Y beam full widths of $\sim$8 and $\sim$12 μm, respectively, as shown

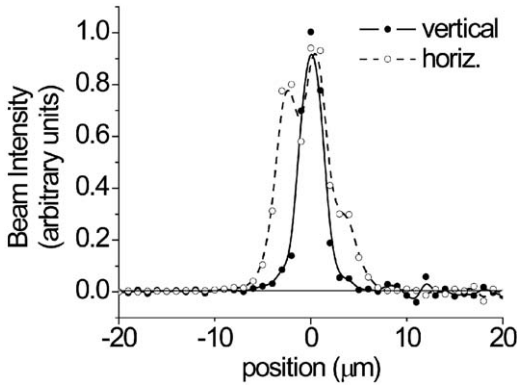

Fig. 4. Horizontal and vertical knife-edge scans through X-ray beam. Position values are difference values calculated using a step interval of 1 μm.

in Fig. 4. An ionization chamber monitored the beam intensity immediately downstream of the beamline monochromator exit slits, and was used to stabilize the beam intensity at the 3D detector by providing feedback to vary the detune of the monochromator second crystal. Data presented below has been corrected for the residual measured variations in beam intensity, which were $<1\%$ over the duration of the entire experiment.

The 3D detector-PCB assembly was rigidly mounted within an electrically screened, metal box that had a light proof, aluminized Mylar X-ray window of thickness 40 μm. This metal box was itself mounted on an $X-Y$ scan stage and visually adjusted so that the estimated centre of the 3D detector was aligned with the beam axis. Output channel 4 of the detector assembly was selected with the multiplexer, and an X line scan begun by microstepping the assembly across the X-ray beam. By monitoring the signal count rate at the MCA, the precise X coordinate of the vertical row of connected electrodes that corresponded to channel 4 of the 3D detector was quickly located. In a like manner, the vertical position of the 3D detector was adjusted to ensure that the beam impinged on the detector mid-way along the vertical row of column electrodes of channel 4. $X-Y$ raster scans of 16×16 points were then made at 10 μm step intervals, measuring successively the response over two horizontally adjacent pixels corresponding to readout channels 3 and 4. The energy histogram data were accumulated by the MCA at each scan position for either 5 or 10 s per point. As depicted in Fig. 2, the overlapping scans of channels 3 and 4 cover the critical inter-pixel boundaries where charge sharing of events occurred. Although no single entire pixel surface area was scanned, the response of the missing data points can be inferred by symmetry. The scans presented below were made with the detector biased at 20 V. Additional scans made at 30 and 40 V bias showed essentially the same results.

4. Results

The contour map of Fig. 5 shows the response of part of the pixel corresponding to readout channel 3. To create this map, for each X, Y coordinate integral counts were made above a lower-level energy threshold cut set at 10 keV for the 256 individual MCA energy spectra files produced during the mesh scan. Energy calibration of the detector was made using its photopeak

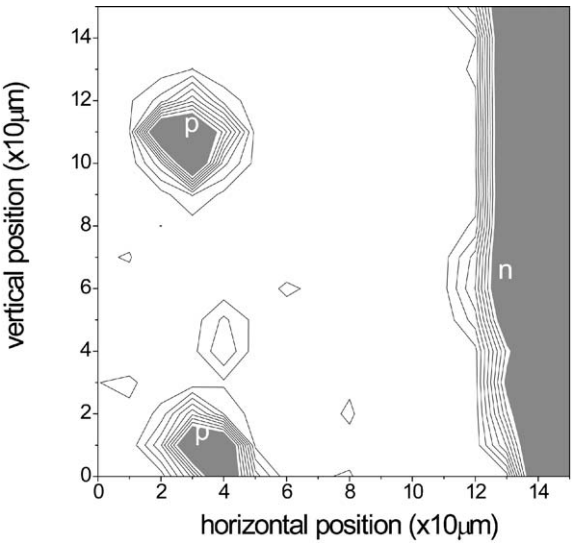

Fig. 5. Response of channel 4 to a vertical–horizontal raster scan at 10 μm step intervals. The contour lines correspond to intensity changes of 3% (of the nominal response 3.4×10^4 counts per scan point for a 5 s integration). The grey filled areas had response $<73\%$ of the nominal response.

response at 12.65 keV. By setting the energy threshold at the high level of 10 keV, the contour map representation is made sensitive to any loss in energy for individual events, for example as a result of incomplete charge collection. The contours clearly define the positions of two vertically adjacent p column electrodes; the fall-off in response at the limit of the vertical pixel boundary to the right; and the outline of the n electrode that is shared at the pixel boundary. Note that within the surface areas occupied by the column electrodes, no or very little X-ray response is seen. This is expected due to an estimated charge carrier lifetime of only nanoseconds within the polycrystalline silicon forming these electrodes, and the lack of any charge-separating, drift field within them. The effective diameter of the electrodes cannot be precisely defined due to the relatively coarse 10 μm sampling interval of the measurement grid (note that the contour lines of Fig. 5 are generated by software interpolation).

Fig. 6 shows the log-scaled histogram of the energy response of channel 3 with the X-ray beam incident at an 'ideal' position, i.e. well inside a pixel boundary and far from p and n columnar electrodes. Here, the detector shows excellent energy response, and the X-ray photopeak is well fitted by a simple Gaussian profile of width 0.91 keV FHHM. The photopeak energy width is dominated by the ASIC charge amplifier electronic noise (the Fano statistical contribution for silicon at this energy is only 0.18 keV FHWM). The absence of any tailing of the peak towards low energies is a stringent test confirming complete charge collection: here, the residual tailing is $<1\%$, and could arise at least in part from diffusely scattered X-rays.

The 3D representation of Fig. 7 shows the response of the two adjacent pixels corresponding to readout channels 3 (left) and 4 (right). To create this map, energy histogram data were summed, with a lower-level threshold set at 6 keV, i.e. about one half the photopeak energy. Channel 3 and 4 spatial response scans were made successively, so Fig. 7 is in fact a composite map made by superposing the data sets. Simple summation of signal counts is possible where the X, Y mesh scan coordinates were duplicated (the scans of channels 3 and 4 overlapped horizontally by 50 μm). This is possible as the electronic noise gave a negligible count contribution of <1 cps above 3 keV. The following features are noted from Fig. 7:

1. The 'counts above threshold' response within the pixel is uniform at a level of precision $\sim 1\%$ except at the columnar electrodes and at the vertical boundary between the pixels of channel A and B. Although this result was expected, this experiment was the first direct confirmation that the fall-off in response is indeed localized at these features on a scale ~ 10 μm (i.e., the limit

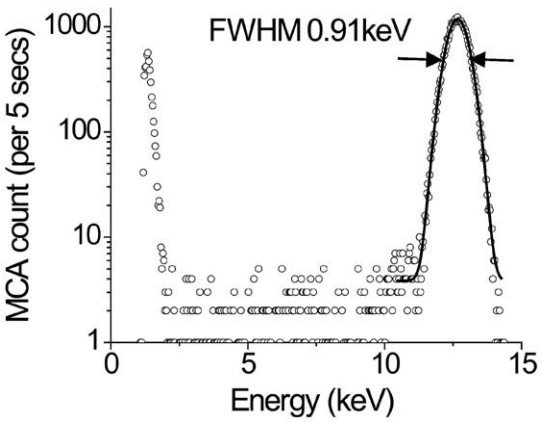

Fig. 6. Spectrum from beam inside pixel boundary (referring to Fig. 5, beam at X, Y coordinates 90 μm, 0 μm) of channel 3. The solid line fit to the photopeak at 12.65 keV is a Gaussian.

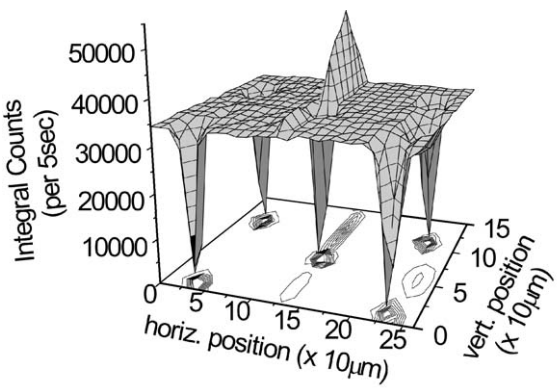

Fig. 7. Composite map from integral counts above an energy threshold of 6 keV, from successive measurements on channels 3 and 4.

in measurement precision imposed by the probing X-ray beam size).

2. With the energy threshold set at 6 keV, there is a vertical strip (at horizontal position ~150 μm) in which count response reaches up to ~60% higher than the surrounding plateau. This is the result of double counting of single X-rays at the vertical pixel boundary, and is the same response that would have been observed if the signals of channels 3 and 4 had been accumulated simultaneously using simple integral counters assigned to each pixel each with an energy threshold set at 6 keV. The relative magnitude of this double counting is strongly dependent upon the precise setting of the 'counting' energy threshold. Fig. 8a is a horizontal section through the 3D plot of Fig. 7 evaluated at the vertical position 120 μm, corresponding to a line that passes through the p electrode centres. The double-count excess at the energy threshold of 6 keV drops to become an equally dramatic deficit as the threshold used in the analysis is increased to 9 keV. This result can be understood by inspection of the energy spectra of Fig. 9, obtained while scanning the X-ray beam along the same horizontal section as that of Fig. 8a. The loss in photopeak counts at horizontal position 40 μm corresponds to a p electrode centre, while the broad 'half energy' bump at horizontal position 140 μm results from almost equal diffusion charge splitting of charge from X-ray events incident at the inter-pixel boundary. Note that at horizontal position 150 μm no events are observed, implying a sharp pixel border response 'cut off' region <20 μm wide.

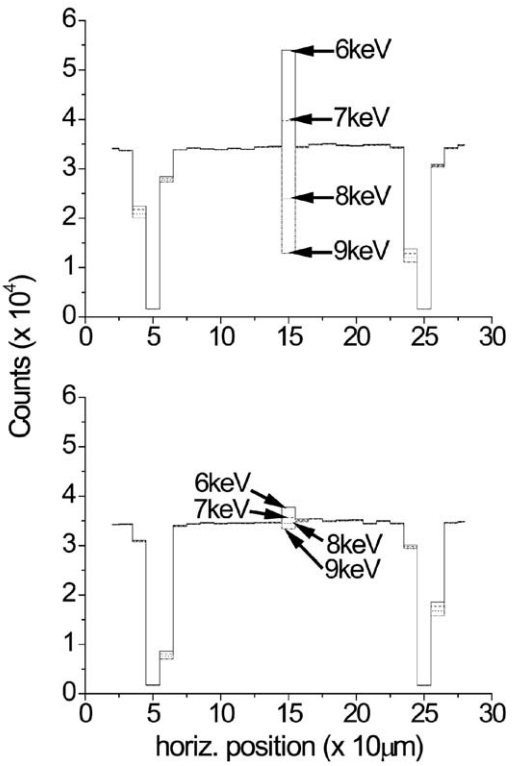

Fig. 8. (a, b) Horizontal line sections through the surface of Fig. 8 passing through the p electrode centres at vertical positions 120 μm (a) and 20 μm (b). Integral count responses are shown for threshold energies 6, 7, 8 and 9 keV.

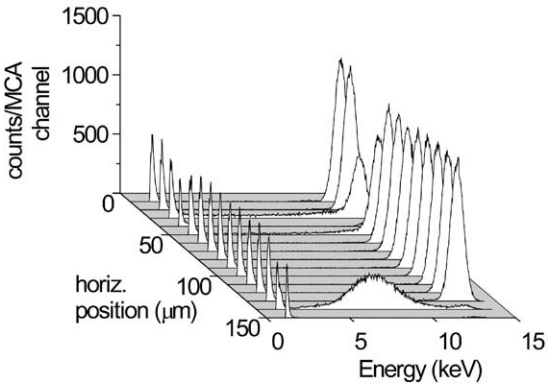

Fig. 9. Energy spectra obtained along the horizontal cut at the vertical position 120 μm. The narrow peaks at <2 keV are the tails of the electronic noise.

Fig. 8b shows the response of a horizontal line section at vertical position 20 μm, i.e., through the nearest neighbour set of p electrodes. This shows a much smaller double count or lost count effect. This apparently conflicting result is believed to result from to the 3D chip having been mounted with a skew error with respect to the vertical axis. A skew angle error of 3° would have resulted in a 5 μm offset between the spatial samplings of the data shown in Figs. 8a and b, while the spatial extent over which charge splitting at

the pixel boundary occurs is apparently $\sim 10\,\mu m$. The spatial sampling interval of $10\,\mu m$ is too low to accurately represent data from a feature of this width. Previously reported measurements of the spatial response of planar pixel detectors at their inter-pixel boundaries [4–6] were also made with X-ray probe beam full widths $> 10\,\mu m$.

3. There is no evidence of a change of count rate as the X-ray beam was scanned vertically across the horizontal boundary between two adjacent pixels. As the p electrodes of these pixels were electrically 'shorted' together in the vertical direction by their aluminium surface traces, the signal charge contributions from the adjacent pixels were analogically summed at the preamplifier stage before the resultant total signal was compared with the 6 keV energy threshold used to generate Fig. 7. Therefore, for the vertically adjacent pixels, the threshold effect on the perceived count rate due to charge splitting between is completely eliminated if all charge carriers are collected from either side of the geometrical pixel boundary.
4. The appearance of a 'depression' in count response between the rightmost two p electrodes is not understood. Inspection of the energy spectrum at the centre of this depression showed tailing to the photopeak signal and the appearance of a distinct peak at energy $\sim 3.5\,keV$. This feature might result from a surface effect (e.g., charge trapping-recombination under the field oxide, itself under a surface aluminium trace) or due to some other some other local artefact. There was no evidence of this count depression at the mirror-symmetric point between the left two p electrodes.

5. Conclusions

We have demonstrated that 3D detectors show excellent charge collection resulting in tail-free energy spectra at the 12.65 keV X-ray energy of interest for protein crystallography measurements. As expected, no X-ray response is within seen at the field-free polycrystalline electrodes of these detectors, but within the resolution limit imposed by the $\sim 10\,\mu m$ probe beam size, these dead areas have been shown not to extend beyond the $20\,\mu m$ diameters of the electrodes themselves. Elsewhere within a pixel, the spectral energy response of the detector is uniform. Charge splitting between adjacent pixels is confined within a band certainly $< 20\,\mu m$ wide, and a uniform response was measured across a horizontal pixel boundary where the split charge was analogically summed, implying no loss of total signal charge. The need for analogue charge summation at pixel boundaries is made clear by the observation of strong modulation in count rate at the vertical pixel boundary where a simple integral counter approach was simulated to analyse the data. Further investigation is required with a smaller probe beam in order to better quantify the inter-pixel boundary areas over which charge splitting is significant, and to investigate the peripheral response of detectors that have recently been fabricated with active edge technology.

Acknowledgements

We are grateful to Mark Rivers and Matt Newville of the GSECARS CAT at the Advanced Photon Source for their essential support at the 13-BMD beamline tests. The development and processing of the 3D silicon detectors was carried out at the Nanofabrication Facility of the Center for Integrated Systems, Stanford University, which is supported by the National Science Foundation. Use of the Advanced Photon Source was supported by the US Department of Energy, Basic Energy Sciences, Office of Science, under Contract No. W-31-109-Eng-38. Continued development of 3DX detectors for protein crystallography applications is being administered by the Molecular Biology Consortium, under a National Institutes of Health, National Center for Research Resources grant 1 R01 RR1 6230-01.

References

[1] J. Morse, C. Kenney, E. Westbrook, I. Naday, S. Parker, Proc. SPIE 4784 (2002) 365.

[2] M. Chmeissani, B. Mikulec, Nucl. Instr. and Meth. A 460 (2001) 81.
[3] Ch. Brönniman, S. Florin, M. Lindner, B. Schmitt, C. Schulze-Briese, J. Synchrotron Radiat. 7 (2000) 301.
[4] J.-F. Bérar, L. Blanquart, N. Boudet, P. Breugnon, B. Caillot, J.-C. Clemens, P. Delpierre, I. Koudobine, C. Mouget, R. Potheau, I. Valin, J. Appl. Cryst. 35 (2002) 471.
[5] C. Ponchut, J.L. Visschers, A. Fornaini, H. Graafsma, M. Mairorino, G. Mettivier, D. Calvet, Nucl. Instr. and Meth. A 484 (2002) 396.
[6] G. Iles, K. Mathieson, P. Murray, S. Passmore, M. Prydderch, P. Seller, S. Thomas, Nucl. Instr. and Meth. A 458 (2001) 427.
[7] Ch. Brönniman, R. Baur, E. Eikenberry, P. Fischer, S. Florin, R. Horisberger, M. Lindner, B. Schmitt, C. Schulze, Nucl. Instr. and Meth. A 477 (2002) 531.
[8] S. Parker, C. Kenney, J. Segal, Nucl. Instr. and Meth. A 395 (1997) 328.
[9] C. Kenney, S. Parker, J. Segal, C. Storment, IEEE Trans. Nucl. Sci. NS-46 (4) (1999) 1224.
[10] C. Kenney, S. Parker, B. Krieger, B. Ludewigt, T. Dubbs, H. Sadrozinski, IEEE Trans. Nucl. Sci. NS-48 (2) (2001) 189.
[11] C. Kenney, S. Parker, E. Walckiers, IEEE Trans. Nucl. Sci. NS-48 (6) (2001) 2405.
[12] Model 3.2 Microslits, Technisches Büro S Fischer, Ober Ramstadt, Germany.